Research Article

Nano Research
2020, 13(3): 768–774

ISSN 1998-0124 CN 11-5974/O4
https://doi.org/10.1007/s12274-020-2692-1

Multi-shelled CuO microboxes for carbon dioxide reduction to ethylene

Dongxing Tan[1,2], Jianling Zhang[1,2,3] (✉), Lei Yao[4], Xiuniang Tan[1,2], Xiuyan Cheng[1,2], Qiang Wan[1,2], Buxing Han[1,2,3], Lirong Zheng[4], and Jing Zhang[4]

[1] *Beijing National Laboratory for Molecular Sciences, CAS Key Laboratory of Colloid, Interface and Chemical Thermodynamics, CAS Research/Education Center for Excellence in Molecular Sciences, Institute of Chemistry, Chinese Academy of Sciences, Beijing 100190, China*
[2] *School of Chemical Sciences, University of Chinese Academy of Sciences, Beijing 100049, China*
[3] *Physical Science Laboratory, Huairou National Comprehensive Science Center, Beijing 101400, China*
[4] *Beijng Synchrotron Radiation Facility (BSRF), Institute of High Energy Physics, Chinese Academy of Sciences, Beijing 100049, China*

Received: 1 December 2019 / **Revised:** 6 January 2020 / **Accepted:** 29 January 2020

ABSTRACT

The electroreduction of CO_2 to valuable chemicals and fuels offers an effective mean for energy storage. Although CO_2 has been efficiently converted into C_1 products (e.g., carbon monoxide, formic acid, methane and methanol), its convention into high value-added multicarbon hydrocarbons with high selectivity and activity still remains challenging. Here we demonstrate the formation of multi-shelled CuO microboxes for the efficient and selective electrocatalytic CO_2 reduction to C_2H_4. Such a structure favors the accessibility of catalytically active sites, improves adsorption of reaction intermediate (CO), inhibits the diffusion of produced OH^- and promotes C–C coupling reaction. Owing to these unique advantages, the multi-shelled CuO microboxes can effectively convert CO_2 into C_2H_4 with a maximum faradaic efficiency of 51.3% in 0.1 M K_2SO_4. This work provides an effective way to improve CO_2 reduction efficiency via constructing micro- and nanostructures of electrocatalysts.

KEYWORDS

multi-shelled CuO microboxes, nanocrystals, CO_2 reduction, C_2H_4

1 Introduction

The excessive emissions of CO_2 have posed a serious threat to the global environment and carbon balance. Using clean energy (electric energy and solar energy) as a driving force to convert CO_2 into chemicals and fuels can not only mitigate greenhouse effect, but also promote carbon cycle [1, 2]. In recent years, great efforts have been devoted to the CO_2 conversion and remarkable achievements have been achieved [3–6]. So far, the efficient conversion of CO_2 into C_1 products [7–17], such as carbon monoxide [4, 10, 12, 15], formic acid [7, 11], and methanol [16, 17], has been well realized. However, converting CO_2 into high value-added multicarbon hydrocarbons (C_{2+}) with high selectivity and activity remains difficult. As is recognized, copper (Cu) is the only metal that can electroreduce CO_2 to C_2H_4, but the selectivity of pure Cu toward C_2H_4 is poor. To overcome this limitation, various strategies have been proposed, including forming alloys of Cu with other metal [18, 19], doping Cu with heteroatoms [20], creating mixture valence states of Cu [21], or designing special electrolytic devices [22, 23]. By taking account of the complexity of these electrocatalysts and electrolytic devices, it is more attractive to develop single electrocatalysts with inherent structures that are desirable for the efficient CO_2 conversion to C_2H_4, but is challenging.

Here we demonstrate the formation of multi-shelled CuO microboxes for the efficient and selective electrocatalytic CO_2 reduction reaction (CO_2 RR) to C_2H_4. The multi-shelled CuO microboxes (~ 1 μm) are constructed by uniform CuO nanocrystals in 19.6 nm. Such a structure favors the accessibility of catalytically active sites and adsorption of reaction intermediate (CO). Moreover, the multi-shelled structure inhibits the diffusion of produced OH^- during CO_2 RR to form a higher pH environment inside CuO microboxes, and the tightly packed CuO nanoparticles could promote C–C coupling reaction, thereby facilitating the conversion efficiency of CO_2 to C_2H_4. Owing to these unique advantages, the as-synthesized multi-shelled CuO microboxes can convert CO_2 into C_2H_4 with a maximum faradaic efficiency of 51.3% in 0.1 M K_2SO_4. This work provides a promising route for improving the efficiency and selectivity of single electrocatalysts for CO_2 conversion to C_{2+} compounds by constructing desirable micro- and nanostructures.

2 Experimental

2.1 Preparation of CuO microboxes and CuO microparticles catalyst

Materials: CO_2 (> 99.999% purity) and N_2 (> 99.99% purity) were provided by Beijing Analysis Instrument Factory. Nafion N117 membrane, Nafion D-521 dispersion, potassium sulfate, potassium bicarbonate, potassium phosphate dibasic anhydrous, L(+)-ascorbic acid and dodecanoic acid were purchased from Beijing InnoChem Science & Technology Co., Ltd. Copper

Address correspondence to zhangjl@iccas.ac.cn

oxide, cuprous oxide, copric chloride dihydrate, polyvinylpyrrolidone (PVP, M_W = 50,000) and nickel oxide were purchased from J&K Scientific Co., Ltd. Absolute ethanol, sodium hydroxide and n-butanol were provided by Beijing Chemical Works. Copper nitrate hydrate and 1,3,5-benzenetricarboxylic acid (BTC) were provided by Sinopharm Chemical Reagent Beijing Co., Ltd.

Preparation of CuO microboxes: In a typical synthesis process, the appropriate amounts of copper nitrate hydrate, 1,3,5-benzenetricarboxylic acid and dodecanoic acid were dispersed in 10 mL of n-butanol and stirred at room temperature for 10 min. Then the solution was transferred into a Teflon liner stainless-steel autoclave, and the autoclave was sealed and heated at 140 °C for 5 h. The solid product was washed with absolute ethanol and dried in a vacuum oven at 80 °C for 24 h. The as-synthesized Cu-BTC was annealed in muffle furnace at 350 °C in air atmosphere for 1 h with a heating rate of 5 °C·min^{-1}. For comparison, the Cu-BTC was annealed in muffle furnace at different temperatures of 250, 300, and 400 °C.

Preparation of CuO microparticles: In a typical synthesis process, the appropriate amounts of copric chloride dihydrate and PVP were dispersed in 100 mL ultrapure water and stirred at room temperature for 30 min to form a homogeneous solution. Next, 10 mL of 2 M sodium hydroxide solution was dropwise added into the solution under magnetic stirring. After 10 min, 10 mL of 0.6 M L(+)-ascorbic acid solution was dropwise added into the mixed solution under magnetic stirring. Then the mixture was kept in 80 °C water bath for 3 h. The as-prepared sample was washed with absolute ethanol and dried in a vacuum oven at 80 °C for 24 h. Finally, the sample was annealed in muffle furnace at 350 °C in air atmosphere for 1 h with a heating rate of 5 °C·min^{-1}.

2.2 Characterizations

The morphologies of the catalysts were characterized by scanning electronic microscopy (SEM, HITACHI S-4800). Transmission electron microscopy (TEM) images were taken on JEOL JEM-EM-1011 and JEOL JEM-2100F field-emission high-resolution transmission electron microscope operated at 200 kV. X-ray diffraction (XRD) patterns were conducted on a Rigaku D/max 2400 diffractometer with Cu Kα radiation (λ = 0.15418 nm) at a scanning rate of 4 °·min^{-1}. The elemental analysis of C and O was performed on a FLASH EA1112 elemental analysis instrument. The content of Cu element was determined by inductively coupled plasma-mass spectrometry (ICP-MS). The X-ray photoelectron spectroscopy (XPS) was carried out with a multipurpose X-ray photoemission spectroscope (Thermo Scientific ESCALAB 250Xi). Thermogravimetric analysis (TGA) was carried out using a PerkinElmer TGA 4000 thermoanalyser under air flow at 5 °C·min^{-1}. The X-ray absorption near-edge structure (XANES) experiment was carried out at Beamline 1W1B at BSRF. Data of X-ray absorption fine structure (XAFS) were processed using the Athena and Artemis programs of thee IFEFFIT package based on FEFF 6. Data were processed with k^3-weighting and an Rbkg value of 1.0. Normalized extended XAFS (EXAFS) data were obtained directly from the Athena program of the IFEFFIT package.

2.3 Fabrication of electrodes

The working electrodes were prepared by loading samples suspension onto the carbon papers (CPs). Briefly, the as-prepared catalyst and 10 μL Nafion D-521 dispersion were dispersed in absolute ethanol and ultra-sonicated for 30 min to form uniform suspension, and the suspension was loaded on the 1 cm × 1 cm CP. The electrode was dried in a vacuum oven at 80 °C for 6 h before the electrochemical experiment.

2.4 Electrochemical impedance spectroscopy (EIS)

The EIS measurement was carried out in 0.5 M $KHCO_3$ at an open circuit potential (OCP) with an amplitude of 5 mV of 10^{-2} to 10^5 Hz.

2.5 Double-layer capacitance (C_{dl})

The C_{dl} was determined by measuring the capacitive current associated with double-layer charging from the scan-rate dependence of cyclic voltammetric stripping. The scan rates were 5, 10, 15, 20, 30, 40 and 50 mV·s^{-1}.

2.6 CO_2 reduction and product analysis

A CHI660E electrochemical analyzer (Shanghai Chenhua instrument co. LTD, China) was used in all the electrochemical experiments. A three electrode test was carried out in a sealed H-cell which was separated by Nafion N117 membrane. The reference and counter electrodes were Ag/AgCl and Pt net (1 cm × 1 cm), respectively. Linear sweep voltammetry (LSV), amperometric *i*–*t* curve and EIS were performed in 0.1 M electrolyte. Before the experiments, the electrolyte solution in the working compartment was bubbling for 1 h with N_2 (99.99%) and CO_2 (99.999%) to form a saturated solution. The pH values of the 0.1 M K_2SO_4 with N_2 and CO_2 are 6.0 and 5.8, respectively. The pH values of the 0.1 M $KHCO_3$ and K_2HPO_4 with CO_2 are 6.8 and 6.5, respectively. The gaseous product in the gas bag was collected and analyzed by gas chromatography (GC, HP 4890D), which was equipped with TCD and FID detectors using helium as the internal standard. The liquid mixture was analyzed by ^{1}H nuclear magnetic resonance (^{1}H NMR), which was recorded on a Bruker Avance III 400 HD spectrometer in deuterium oxide-d_2 with TMS as an internal standard. All the experiments were measured at atmospheric pressure and room temperature and all potentials reported in this paper were with respect to reversible hydrogen electrode (RHE).

All the potentials were converted to the RHE using Eq. (1) by considering the pH of the solution.

$$\text{Potential in RHE} = \text{Applied potential vs. Ag/AgCl} + 0.21\ \text{V} + 0.0592 \times \text{pH} \quad (1)$$

The faradaic efficiency of each product was calculated according to the Eq. (2).

$$\text{FE} = \frac{N_i \cdot n \cdot F}{Q} \quad (2)$$

where Q: the total charge, C; N_i: the number of moles for specific product, mol; n: the number of electrons exchanged for specific product, which is 12 for C_2H_4, 2 for CO, HCOOH and H_2; F: Faradaic constant, which is 96,485 C·mol^{-1}.

2.7 Regeneration of used catalyst

The used working electrode was annealed in muffle furnace at 350 °C in air atmosphere for 0.5 h with a heating rate of 5 °C min^{-1}.

3 Results and discussion

To get the target product, the cubic crystals of metal-organic framework Cu-BTC was first synthesized (see its characterizations in Fig. S1–S3 in the Electronic Supplementary Material (ESM)), followed by calcination at a certain temperature for 1 h (Fig. 1(a)). As an example, Figs. 1(b)–1(g) show the characterizations of the product obtained by heating Cu-BTC at 350 °C. SEM

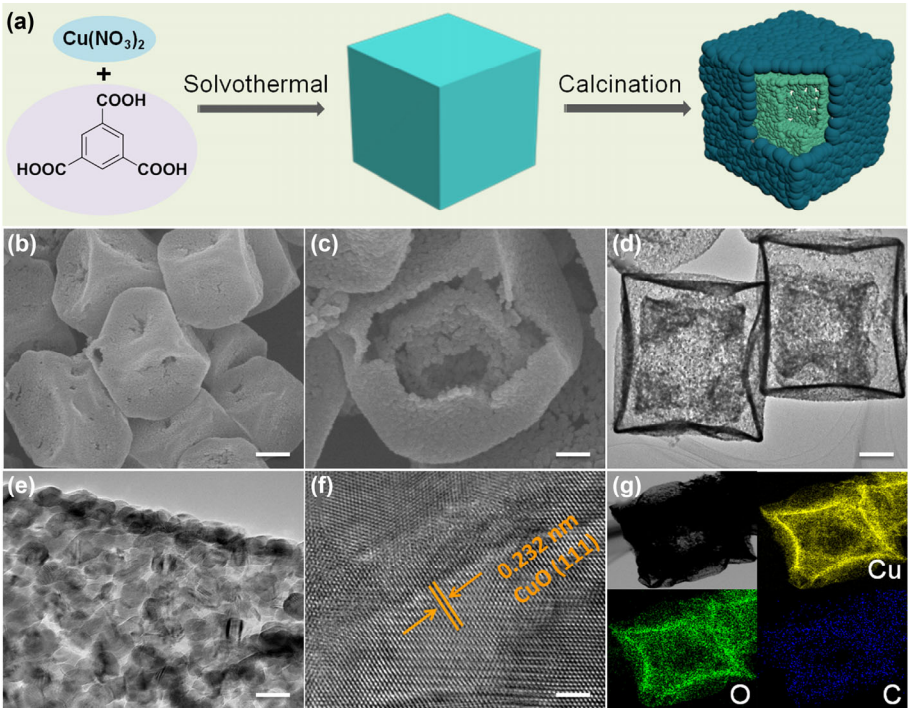

Figure 1 Schematic illustration of the synthetic process of CuO microboxes (a). SEM images (b) and (c), TEM images (d) and (e), HRTEM image (f) and EDX mapping (g) of CuO microboxes. Scale bars, 300 nm in (b), 150 nm in (c), 200 nm in (d), 20 nm in (e), 2 nm in (f)

image shows that the product basically maintains the cubic morphology of Cu-BTC (Fig. 1(b)). However, it has a multi-shelled hollow structure, as can be seen from the SEM image of the cracked cube and TEM image (Figs. 1(c) and 1(d)). The magnified TEM image reveals that the hollow microbox is constructed by CuO nanocrystals with a diameter of ~ 19.6 nm (Fig. 1(e) and Fig. S4 in the ESM). The typical lattice fringe of the product has an interplanar distance of 0.232 nm (Fig. 1(f)), corresponding to the crystal plane spacing of (111) plane of monoclinic phase CuO [24]. It is consistent with the result of XRD (Fig. S5 in the ESM). Energy dispersive X-ray elemental (EDX) mapping images show that Cu, O and C elements evenly distribute in the whole sample (Fig. 1(g)). The Cu content was determined to be 77.8 wt.% by ICP-MS. The contents of O and C are 19.9 wt.% and 2.3 wt.%, respectively, as determined by elemental analysis.

XPS was used to characterize the surface chemical compositions and bonding configurations of the multi-shelled CuO microboxes. The high-resolution Cu 2p spectrum (Fig. 2(a)) shows the binding energies at 933.9 and 953.9 eV, which are characteristic for $2p_{3/2}$ and $2p_{1/2}$ of Cu^{2+} in CuO [25, 26], respectively. In the high-resolution O 1s spectrum, the binding energies at 529.8, 531.6 and 533.0 eV correspond to O–Cu, O–H and O–C [27, 28], respectively (Fig. 2(b)). The high-resolution C 1s spectrum (Fig. S6 in the ESM) shows three peaks at 284.8, 286.5 and 288.8 eV, which correspond to C–C/C=C, C–O and C=O [4, 29], respectively. The remaining carbon can effectively maintain the integrity of microboxes in the catalytic process, thereby improving the electrocatalytic stability [29]. Synchrotron EXAFS was used to get more detailed

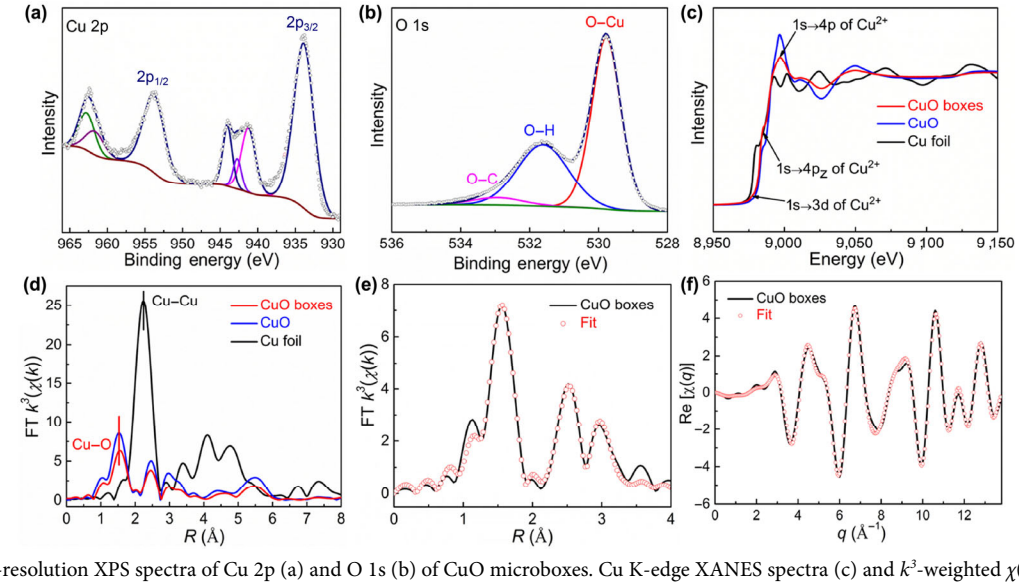

Figure 2 High-resolution XPS spectra of Cu 2p (a) and O 1s (b) of CuO microboxes. Cu K-edge XANES spectra (c) and k^3-weighted $\chi(k)$ function of the EXAFS spectra (d). Cu foil and CuO were used as contrast samples. EXAFS fitting curves of CuO microboxes in R space (e) and in q space (f).

structural information of multi-shelled CuO microboxes. The XANES of the Cu K-edge of the CuO microboxes catalyst exhibits similar spectrum features to that of the reference CuO (Fig. 2(c)). The well-defined peaks at 8,977, 8,985 and 8,997 eV correspond to the 1s → 3d, 1s → 4p_z and 1s → 4p features of Cu^{2+}, respectively. It indicates that the multi-shelled CuO microboxes possess similar conformation as CuO, coinciding well with XRD result [30]. The Fourier transform (FT) k^3-weighted $\chi(k)$ function of the EXAFS spectrum for CuO microboxes exhibits dominant Cu–O coordination with a peak at 1.55 Å, similar to that of reference CuO (Fig. 2(d)). The quantitative EXAFS curve fitting analysis was further used to investigate the coordination configuration of CuO microboxes (Figs. 2(e) and 2(f)). The best-fitting analysis reveals that the coordination number of the multi-shelled CuO microboxes is lower than that of reference CuO (Tables S1 and S2 in the ESM). The unsaturated coordination structure enables the multi-shelled CuO microboxes to have more active sites, which are favorable for improving catalytic efficiency for CO_2 RR [31].

The catalytic abilities of the multi-shelled CuO microboxes towards CO_2 reduction were evaluated by LSV in N_2 and CO_2 saturated 0.1 M K_2SO_4, respectively. For comparison, the CuO solid particles with the similar particle size as the multi-shelled CuO microboxes were prepared by a surfactant-assisted method (Fig. S7 in the ESM). In the CO_2 saturated 0.1 M K_2SO_4 (Fig. 3(a)), the current densities of CuO microboxes and CuO particles were obviously higher than those in N_2 saturated electrolyte. It indicates that the catalysts are more favorable for CO_2 RR than hydrogen evolution reaction (HER) [4]. Moreover, the current density of the multi-shelled CuO microboxes is much higher than that of CuO particles at relatively high applied potential region. For example, the current densities of the multi-shelled CuO microboxes and solid particles are 61.9 and 27.9 mA·cm^{-2} at −1.4 V, respectively. GC and ^{1}H NMR spectroscopy were used to analyze the gaseous products and liquid products formed in CO_2 RR, respectively. The reduction products and the corresponding faradaic efficiencies are shown in Fig. 3(b). As shown in Fig. 3(b) and Fig. S8 in the ESM, C_2H_4, CO and HCOOH are reduction products, accompanied with H_2 from HER. It is noted that the selectivities of the products change with the applied potentials. With the increase of applied potential, the faradaic efficiency of C_2H_4 (FE(C_2H_4)) increases first and then decreases. When the applied potential is −1.05 V vs. RHE, the FE(C_2H_4) reaches the maximum of 49.6%, with a high current density of 27.7 mA·cm^{-2}, and the total hydrocarbon faradaic efficiency is up to 72%. In contrast, the CuO solid particles exhibit poor reduction efficiency of CO_2 with a low total hydrocarbon faradaic efficiency of 33.5% and current density (15.9 mA·cm^{-2}), and the FE(C_2H_4) is only 19.9% at the same applied potential (Fig. S9 in the ESM). Furthermore, the catalytic performance of the multi-shelled CuO microboxes is comparable or even better than those of the reported Cu-based catalysts at similar experimental conditions, e.g., Cu(B)-2 [20], Cu-on-Cu_3N [21], anodized Cu [32], and redeposited Cu [33] (Table S3 in the ESM). Figure 3(c) shows the total current densities and partial current densities of C_2H_4 at different applied potentials. The current density of C_2H_4 increases first and then keeps nearly unchanged with the increasing applied potential.

The catalytic stability of the multi-shelled CuO microboxes for CO_2 RR was examined under −1.05 V for 10 h in 0.1 M K_2SO_4 (Fig. 3(d)). Along with the reduction process, the current density increases gradually and then tends to be unchanged, while the FE(C_2H_4) increases first in the initial stage and decreases slightly. The FE(C_2H_4) reaches a maximum value of 51.3% when the reduction time is 1.5 h. The composition and valence states

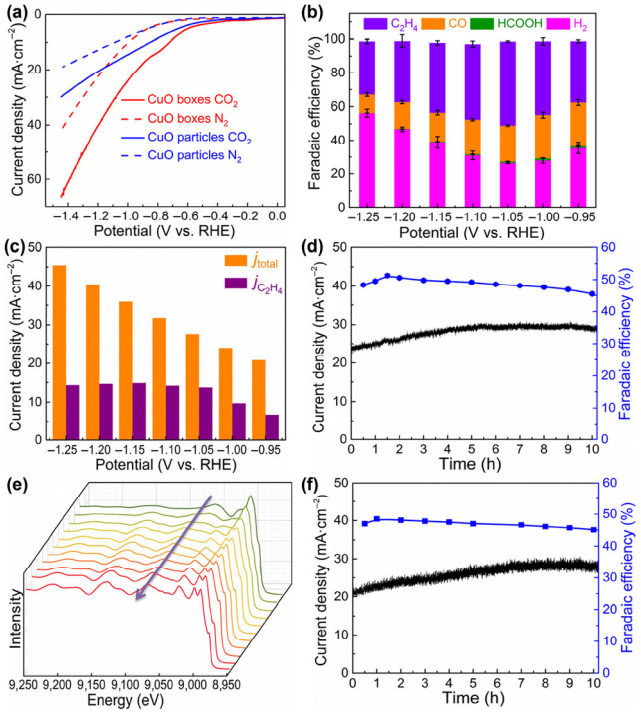

Figure 3 LSV curves acquired in N_2-saturated (dotted line) or CO_2-saturated (solid line) 0.1 M K_2SO_4 solution at a scan rate of 50 mV·s^{-1} (a). Faradaic efficiencies for C_2H_4, CO, HCCOH and H_2 of CuO microboxes at different applied potentials (b). Total current densities and partial current densities of C_2H_4 at different applied potentials (c). Stability of CuO microboxes at a potential of −1.05 V vs. RHE (d). *In-situ* Cu K-edge EXAFS spectra of CuO microboxes during electrolysis (e). The arrow direction: 0, 5, 10, 30, 60, 90, 120, 180, 240, 600 min and Cu foil. Stability of re-oxidized CuO microboxes at a potential of −1.05 V vs. RHE during 10 h (f).

of metal on the surface of CuO microboxes at this moment were analyzed by XRD and XPS (Fig. S10 in the ESM). The XRD results reveal that the catalyst mainly consists of metallic Cu and a small amount of Cu_2O, while the XPS shows that the valence states of Cu on the surface of CuO microboxes are mainly Cu(+) and Cu(0). To get further information on the change of the composition and valence states of CuO microboxes during CO_2 RR, the *in-situ* EXAFS characterization of the reaction process was performed. As shown in Fig. 3(e), CuO is gradually reduced to metallic Cu as the reduction proceeds, which is responsible for the gradual increase in current density in Fig. 3(d). Furthermore, the accumulation of HCOOH in the electrolyte during CO_2 RR reduces the pH value of the electrolyte, which can reduce the FE(C_2H_4). The catalyst after CO_2 reduction at −1.05 V for 10 h was characterized by TEM and XRD (Fig. S11 in the ESM). The initial morphology of microboxes was basically maintained, but CuO was reduced to metallic Cu. Then the regeneration of the used catalyst was studied. By a re-oxidization in air for 0.5 h, the used catalyst can be easily converted back to CuO (Fig. S12 in the ESM) and regains the performance of the fresh CuO microboxes (Fig. 3(f)). Therefore, the CuO microboxes have good recyclability for practical electrolysis application.

The Brunauer–Emmett–Teller (BET) surface area (Fig. S13(a) in the ESM) and electrochemical surface area (ECSA) of CuO microboxes and CuO solid particles were compared. ECSA can be evaluated by comparing the C_{dl} of catalysts (Fig. 4(a)) [4, 34]. The BET surface area and the C_{dl} of CuO microboxes are obviously higher than that of CuO particles. The larger ECSA not only provides more abundant active sites, but also enhances the CO_2 adsorption capacity [35]. The CO_2 adsorption isotherms of CuO microboxes and CuO particles were

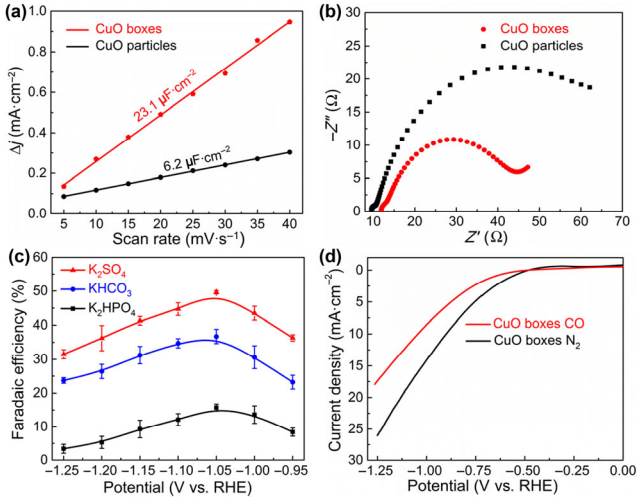

Figure 4 Charging current density differences Δj plotted against scan rates (a). Simulated EIS spectra of the CuO microboxes and CuO particles (b). FE(C_2H_4) at different applied potentials in different electrolytes as catalyzed by CuO microboxes (c). LSV curves acquired in CO saturated (red line) or N_2 saturated (black line) 0.1 M NaF solution at a scan rate of 50 mV·s^{-1} (d).

determined (Fig. S13(b) in the ESM). The CO_2 adsorption capacity of CuO microboxes (35.2 mg·g^{-1}) at 298 K and 1 atm is ~ 4 times as that of CuO particles (8.9 mg·g^{-1}). The EIS was used to gain an insight into reaction kinetics of CO_2 RR. The EIS was carried out in 0.1 M K_2SO_4 (Fig. S14(a) in the ESM) and the electrical equivalent circuit (Fig. S14(b) in the ESM) was used to fit the impedance data. The Nyquist plots confirm that CuO microboxes possess smaller charge transfer resistance than CuO particles (Fig. 4(b)). It indicates a faster electron transfer process for CuO microboxes during CO_2 RR [36]. The large ECSA, high CO_2 adsorption capacity and small charge transfer resistance of the CuO microboxes promote CO_2 adsorption and electron transfer on the electrode surface, thus facilitating the CO_2 RR to C_2H_4 [37].

The effect of electrolyte on catalytic efficiency of CuO microboxes was studied by using K_2SO_4, $KHCO_3$ and K_2HPO_4. As shown in Fig. 4(c), the FE(C_2H_4) in K_2SO_4 electrolyte is obviously higher than that in $KHCO_3$ and K_2HPO_4. In the process of reducing CO_2 to C_2H_4 ($2CO_2 + 8H_2O + 12e^- \rightarrow C_2H_4 + 12OH^-$), a large number of OH^- ions are produced near the catalyst/electrolyte interface [38], which can be neutralized by HPO_4^{2-} or HCO_3^- due to their strong buffer capacity [39]. However, SO_4^{2-} does not have any buffering effect to neutralize OH^-, resulting in the high local pH near the catalyst/electrolyte interface, which is more conducive to reduce CO_2 to C_2H_4 [39–41]. On the other hand, compared with CuO particles, the multi-shelled structure of CuO microboxes could effectively inhibit the diffusion of OH^- due to cage effect, thus forming a higher pH environment within the CuO microboxes, thereby improving the conversion efficiency of CO_2 to C_2H_4.

CO is considered to be an important intermediate in the reduction of CO_2 to C_2H_4 [20, 39, 42]. If the catalyst can effectively stabilize the CO intermediate, it is more favorable to achieve C–C coupling and then to produce C_2H_4. Figure 4(d) shows the LSV curves of multi-shelled CuO microboxes in CO and N_2 saturated NaF solution. Notably, the onset potential of multi-shelled CuO microboxes in CO saturated electrolyte is more negative than that in N_2 saturated electrolyte. It can be attributed to the effective binding energy and stronger adsorption affinity of CO by CuO microboxes [43]. Therefore, the catalyst can effectively stabilize the active intermediate and then produce C_2H_4 by C–C coupling.

The formation of the highly active multi-shelled CuO microboxes from Cu-BTC is very interesting. To well understand its formation process, Cu-BTC was heated at different temperatures. The product treated at 250 °C remained the original morphology and crystal structure of Cu-BTC (Fig. S15 in the ESM and Fig. 5(a)). When the calcination temperature was 300 °C, the multi-shelled CuO microboxes were formed, similar to those synthesized at 350 °C. At 400 °C, the cubic structure collapsed, which is caused by the complete loss of organic compositions as evidenced by thermogravimetric analysis (Fig. S16 in the ESM). It means that the existence of a suitable amount of carbon is necessary for stabilizing the multi-shelled microbox structure. The formation of multi-shelled CuO microboxes by heating at temperatures higher than 300 °C can be attributed to the heterogeneous contraction during the calcination process in air, with a large weight loss and temperature gradient from outside to inside [44, 45].

The electrocatalytic performances of the catalysts calcined at different temperatures were measured. The multi-shelled CuO microboxes calcined at 350 °C have the highest current density at the same potential (Fig. 5(b)) and the best CO_2 reduction performance (Fig. 5(c)). For example, the current densities at –1.0 V of the products obtained at 250, 300, 400 and 350 °C are 10.5, 14.1, 18.6 and 24.2 mA·cm^{-2}. Meanwhile, the FE(C_2H_4) values of the products obtained at 250, 300, 400 and 350 °C are 12.1%, 26.3%, 44.3% and 49.6% at –1.05 V, respectively. As discussed above, the heating at lower or higher temperature for Cu-BTC can cause the existence of more organic compositions or destruction of the multi-shelled structure, respectively, which are both unfavorable for CO_2 RR to C_2H_4. EIS was used to further explain the difference of reaction kinetics among the catalysts calcined from Cu-BTC at different temperatures (Fig. S17 in the ESM). CuO microboxes calcined at 350 °C possess smaller charge transfer resistance than that of the catalysts calcined at other temperatures. This indicates a faster electron transfer process in the CO_2 RR for CuO microboxes obtained at 350 °C. Meanwhile, the ECSA of the products obtained at different temperatures were determined. The results show that the ECSA of CuO microboxes obtained at 350 °C (23.1 μF·cm^{-2}) is ~ 1.8, 1.6, 1.2 times as that of the products obtained at 250 °C (12.9 μF·cm^{-2}), 300 °C (14.2 μF·cm^{-2}) and

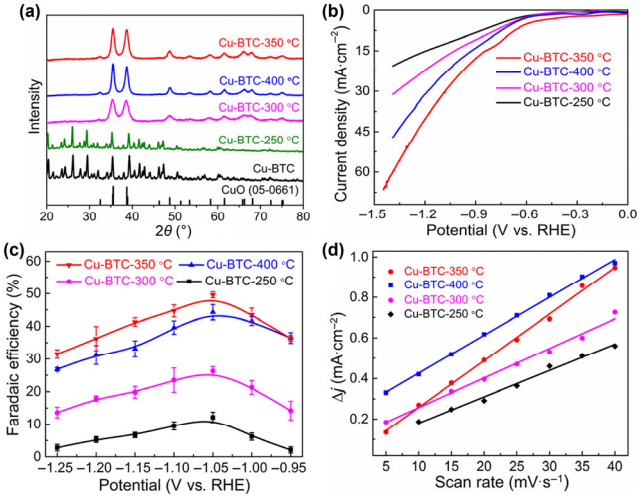

Figure 5 XRD patterns of the catalysts calcined from Cu-BTC at different temperatures (a). The standard diffraction pattern for CuO (JCPDS no. 05-0661) is provided as reference. LSV curves for acquired in CO_2-saturated 0.1 M K_2SO_4 solution at a scan rate of 50 mV·s^{-1} (b). FE(C_2H_4) of the catalysts calcined from Cu-BTC at different temperatures (c). Charging current density differences Δj plotted against scan rates for the catalysts calcined from Cu-BTC at different temperatures (d).

400 °C (18.7 μF·cm^{-2}), respectively (Fig. 5(d)). Clearly, the CuO microboxes obtained at 350 °C has the highest ECSA and more catalytically active sites, which is favorable for stabilizing active intermediate (CO) and achieving C–C coupling to produce C_2H_4. Therefore, the CuO microboxes obtained at 350 °C show the highest reduction efficiency of CO_2.

4 Conclusions

We demonstrate the formation of multi-shelled CuO microboxes electrocatalyst constructed by small and uniform CuO nanocrystals (~ 19.6 nm). Compared with the ordinary CuO microparticles, the efficiency of converting CO_2 into C_2H_4 by multi-shelled CuO microboxes can be significantly improved. It exhibits a maximum faradaic efficiency to C_2H_4 of 51.3% at −1.05 V. This work provides an effective way to improve CO_2 RR efficiency via constructing micro- and nanostructures of electrocatalysts. We anticipate that more single electrocatalysts with inherent structures that are desirable for highly efficient and selective CO_2 reduction to C_2H_4 would be explored in future.

Acknowledgements

We thank the financial supports from Ministry of Science and Technology of China (No. 2017YFA0403003), the National Natural Science Foundation of China (Nos. 21525316 and 21673254), Chinese Academy of Sciences (No. QYZDY-SSW-SLH013) and Beijing Municipal Science & Technology Commission (No. Z191100007219009).

Electronic Supplementary Material: Supplementary material (SEM and TEM images; XRD spectra; XPS spectra; ^{1}H NMR spectra and so on) is available in the online version of this article at https://doi.org/10.1007/s12274-020-2692-1.

References

[1] Wu, J. H.; Huang, Y.; Ye, W.; Li, Y. G. CO_2 reduction: From the electrochemical to photochemical approach. *Adv. Sci.* **2017**, *4*, 1700194.

[2] Yu, X. X.; Yang, Z. Z.; Qiu, B.; Guo, S. E.; Yang, P.; Yu, B.; Zhang, H. Y.; Zhao, Y. F.; Yang, X. Z.; Han, B. X. et al. Eosin Y-functionalized conjugated organic polymers for visible-light-driven CO_2 reduction with H_2O to CO with high efficiency. *Angew. Chem., Int. Ed.* **2019**, *58*, 632–636.

[3] Yang, H. B.; Hung, S. F.; Liu, S.; Yuan, K. D.; Miao, S.; Zhang, L. P.; Huang, X.; Wang, H. Y.; Cai, W. Z.; Chen, R. et al. Atomically dispersed Ni(I) as the active site for electrochemical CO_2 reduction. *Nat. Energy* **2018**, *3*, 140–147.

[4] Tan, D. X.; Zhang, J. L.; Cheng, X. Y.; Tan, X. N.; Shi, J. B.; Zhang, B. X.; Han, B. X.; Zheng, L. R.; Zhang, J. Cu_xNi_y alloy nanoparticles embedded in a nitrogen-carbon network for efficient conversion of carbon dioxide. *Chem. Sci.* **2019**, *10*, 4491–4496.

[5] Zhang, W. J.; Hu, Y.; Ma, L. B.; Zhu, G. Y.; Wang, Y. R.; Xue, X. L.; Chen, R. P.; Yang, S. Y.; Jin, Z. Progress and perspective of electrocatalytic CO_2 reduction for renewable carbonaceous fuels and chemicals. *Adv. Sci.* **2018**, *5*, 1700275.

[6] Hursán, D.; Samu, A. A.; Janovák, L.; Artyushkova, K.; Asset, T.; Atanassov, P.; Janáky, C. Morphological attributes govern carbon dioxide reduction on N-doped carbon electrodes. *Joule* **2019**, *3*, 1719–1933.

[7] Yang, H.; Han, N.; Deng, J.; Wu, J. H.; Wang, Y.; Hu, Y. P.; Ding, P.; Li, Y. F.; Li, Y. G.; Lu, J. Selective CO_2 reduction on 2D mesoporous Bi nanosheets. *Adv. Energy Mater.* **2018**, *8*, 1801536.

[8] Choi, Y. W.; Scholten, F.; Sinev, I.; Roldan Cuenya, B. Enhanced stability and CO/Formate selectivity of plasma-treated SnO_x/AgO_x catalysts during CO_2 electroreduction. *J. Am. Chem. Soc.* **2019**, *141*, 5261–5266.

[9] Li, Q.; Fu, J. J.; Zhu, W. L.; Chen, Z. Z.; Shen, B.; Wu, L. S.; Xi, Z.; Wang, T. Y.; Lu, G.; Zhu, J. J. et al. Tuning Sn-catalysis for electrochemical reduction of CO_2 to CO via the core/shell Cu/SnO_2 structure. *J. Am. Chem. Soc.* **2017**, *139*, 4290–4293.

[10] Jiao, J. Q.; Lin, R.; Liu, S. J.; Cheong, W.; Zhang, C.; Chen, Z.; Pan, Y.; Tang, J. G.; Wu, K. L.; Hung, S. F. et al. Copper atom-pair catalyst anchored on alloy nanowires for selective and efficient electrochemical reduction of CO_2. *Nat. Chem.* **2019**, *11*, 222–228.

[11] Zheng, X. L.; Ji, Y. F.; Tang, J.; Wang, J. Y.; Liu, B. F.; Steinrück, H. G.; Lim, K.; Li, Y. Z.; Toney, M. F.; Chan, K. R. et al. Theory-guided Sn/Cu alloying for efficient CO_2 electroreduction at low overpotentials. *Nat. Catal.* **2019**, *2*, 55–61.

[12] Tan, D. X.; Cui, C. N.; Shi, J. B.; Luo, Z. X.; Zhang, B. X.; Tan, X. N.; Han, B. X.; Zheng, L. R.; Zhang, J.; Zhang, J. L. Nitrogen-carbon layer coated nickel nanoparticles for efficient electrocatalytic reduction of carbon dioxide. *Nano Res.* **2019**, *12*, 1167–1172.

[13] Sun, X. F.; Chen, C. J.; Liu, S. J.; Hong, S.; Zhu, Q. G.; Qian, Q. L.; Han, B. X.; Zhang, J.; Zheng, L. R. Aqueous CO_2 reduction with high efficiency using α-$Co(OH)_2$-supported atomic Ir electrocatalysts. *Angew. Chem., Int. Ed.* **2019**, *58*, 4669–4673.

[14] Zhao, C. M.; Dai, X. Y.; Yao, T.; Chen, W. X.; Wang, X. Q.; Wang, J.; Yang, J.; Wei, S. Q.; Wu, Y.; Li, Y. D. Ionic exchange of metal-organic frameworks to access single nickel sites for efficient electroreduction of CO_2. *J. Am. Chem. Soc.* **2017**, *139*, 8078–8081.

[15] Zhang, B. X.; Zhang, J. L.; Shi, J. B.; Tan, D. X.; Liu, L. F.; Zhang, F. Y.; Lu, C.; Su, Z. Z.; Tan, X. N.; Cheng, X. Y. et al. Manganese acting as a high-performance heterogeneous electrocatalyst in carbon dioxide reduction. *Nat. Commun.* **2019**, *10*, 2980.

[16] Lu, L.; Sun, X. F.; Ma, J.; Yang, D. X.; Wu, H. H.; Zhang, B. X.; Zhang, J. L.; Han, B. X. Highly efficient electroreduction of CO_2 to methanol on palladium-copper bimetallic aerogels. *Angew. Chem., Int. Ed.* **2018**, *57*, 14149–14153.

[17] Yang, D. X.; Zhu, Q. G.; Chen, C. J.; Liu, H. Z.; Liu, Z. M.; Zhao, Z. J.; Zhang, X. Y.; Liu, S. J.; Han, B. X. Selective electroreduction of carbon dioxide to methanol on copper selenide nanocatalysts. *Nat. Commun.* **2019**, *10*, 677.

[18] Mi, Y. Y.; Peng, X. Y.; Liu, X. J.; Luo, J. Selective formation of C_2 products from electrochemical CO_2 reduction over $Cu_{1.8}Se$ nanowires. *ACS Appl. Energy Mater.* **2018**, *1*, 5119–5123.

[19] Hoang, T. T. H.; Verma, S.; Ma, S. C.; Fister, T. T.; Timoshenko, J.; Frenkel, A. I.; Kenis, P. J. A.; Gewirth, A. A. Nanoporous copper-silver alloys by additive-controlled electrodeposition for the selective electroreduction of CO_2 to ethylene and ethanol. *J. Am. Chem. Soc.* **2018**, *140*, 5791–5797.

[20] Zhou, Y. S.; Che, F. J.; Liu, M.; Zou, C. Q.; Liang, Z. Q.; de Luna, P.; Yuan, H. F.; Li, J.; Wang, Z. Q.; Xie, H. P. et al. Dopant-induced electron localization drives CO_2 reduction to C_2 hydrocarbons. *Nat. Chem.* **2018**, *10*, 974–980.

[21] Liang, Z. Q.; Zhuang, T. T.; Seifitokaldani, A.; Li, J.; Huang, C. W.; Tan, C. S.; Li, Y.; de Luna, P.; Dinh, C. T.; Hu, Y. F. et al. Copper-on-nitride enhances the stable electrosynthesis of multi-carbon products from CO_2. *Nat. Commun.* **2018**, *9*, 3828.

[22] Lv, J. J.; Jouny, M.; Luc, W.; Zhu, W. L.; Zhu, J. J.; Jiao, F. A highly porous copper electrocatalyst for carbon dioxide reduction. *Adv. Mater.* **2018**, *30*, 1803111.

[23] Dinh, C. T.; Burdyny, T.; Kibria, M.; Seifitokaldani, A.; Gabardo, C. M.; García de Arquer, F.; Kiani, A.; Edwards, J. P.; de Luna, P.; Bushuyev, O. S. et al. CO_2 Electroreduction to ethylene via hydroxide-mediated copper catalysis at an abrupt interface. *Science* **2018**, *360*, 783−787.

[24] Amaniampong, P. N.; Trinh, Q. T.; Wang, B.; Borgna, A.; Yang, Y. H.; Mushrif, S. H. Biomass oxidation: Formyl C–H bond activation by the surface lattice oxygen of regenerative CuO nanoleaves. *Angew. Chem., Int. Ed.* **2015**, *54*, 8928–8933.

[25] Dang, R.; Jia, X. L.; Liu, X.; Ma, H. T.; Gao, H. Y.; Wang, G. Controlled synthesis of hierarchical Cu nanosheets@CuO nanorods as high-performance anode material for lithium-ion batteries. *Nano Energy* **2017**, *33*, 427–435.

[26] Li, W.; Feng, X. L.; Zhang, Z.; Jin, X.; Liu, D. P.; Zhang, Y. A controllable surface etching strategy for well-defined spiny yolk@shell CuO@CeO_2 cubes and their catalytic performance boost. *Adv. Funct. Mater.* **2018**, *28*, 1802559.

[27] Wang, F.; He, X. X.; Sun, L. M.; Chen, J. Q.; Wang, X. J.; Xu, J. H.; Han, X. G. Engineering an N-doped TiO_2@N-doped C butterfly-like nanostructure with long-lived photo-generated carriers for efficient photocatalytic selective amine oxidation. *J. Mater. Chem. A* **2018**, *6*, 2091–2099.

[28] Zubir, N. A.; Yacou, C.; Motuzas, J.; Zhang, X. W.; Zhao, X. S.; Diniz da Costa, J. C. The sacrificial role of graphene oxide in stabilising a Fenton-like catalyst GO-Fe_3O_4. *Chem. Commun.* **2015**, *51*, 9291–9293.

[29] Kim, A. Y.; Kim, M. K.; Cho, K.; Woo, J.; Lee, Y.; Han, S. H.; Byun, D.; Choi, W.; Lee, J. K. One-step catalytic synthesis of CuO/Cu_2O in a graphitized porous C matrix derived from the cu-based metal-organic framework for Li- and Na-ion batteries. *ACS Appl. Mater. Interfaces* ***2016***, *8*, 19514–19523.

[30] Groothaert, M. H.; van Bokhoven, J. A.; Battiston, A. A.; Weckhuysen, B. M.; Schoonheydt, R. A. Bis(μ−oxo)dicopper in Cu-ZSM-5 and its role in the decomposition of NO: A combined *in situ* XAFS, UV–Vis–near-IR, and kinetic study. *J. Am. Chem. Soc.* **2003**, *125*, 7629–7640.

[31] Gu, Z. X.; Yang, N.; Han, P.; Kuang, M.; Mei, B. B.; Jiang, Z.; Zhong, J.; Li, L.; Zheng, G. F. Oxygen vacancy tuning toward efficient electrocatalytic CO_2 reduction to C_2H_4. *Small Methods* **2019**, *3*, 1800449.

[32] Lee, S. Y.; Jung, H.; Kim, N. K.; Oh, H. S.; Min, B. K.; Hwang, Y. J. Mixed copper states in anodized Cu electrocatalyst for stable and selective ethylene production from CO_2 reduction. *J. Am. Chem. Soc.* **2018**, *140*, 8681–8689.

[33] de Luna, P.; Quintero-Bermudez, R.; Dinh, C. T.; Ross, M. B.; Bushuyev, O. S.; Todorović, P.; Regier, T.; Kelley, S. O.; Yang, P. D.; Sargent, E. H. Catalyst electro-redeposition controls morphology and oxidation state for selective carbon dioxide reduction. *Nat. Catal.* **2018**, *1*, 103–110.

[34] Gao, S.; Lin, Y.; Jiao, X. C.; Sun, Y. F.; Luo, Q. Q.; Zhang, W. H.; Li, D. Q.; Yang, J. L.; Xie, Y. Partially oxidized atomic cobalt layers for carbon dioxide electroreduction to liquid fuel. *Nature* **2016**, *529*, 68–71.

[35] Tan, X. Y.; Yu, C.; Zhao, C. T.; Huang, H. W.; Yao, X. C.; Han, X. T.; Guo, W.; Cui, S.; Huang, H. L.; Qiu, J. S. Restructuring of Cu_2O to Cu_2O@Cu-metal–organic frameworks for selective electrochemical reduction of CO_2. *ACS Appl. Mater. Interfaces* **2019**, *11*, 9904–9910.

[36] Li, X. G.; Bi, W. T.; Chen, M. L.; Sun, Y. X.; Ju, H. X.; Yan, W. S.; Zhu, J. F.; Wu, X. J.; Chu, W. S.; Wu, C. Z. et al. Exclusive Ni-N_4 sites realize near-unity CO selectivity for electrochemical CO_2 reduction. *J. Am. Chem. Soc.* **2017**, *139*, 14889–14892.

[37] Ju, W.; Bagger, A.; Hao, G. P.; Varela, A. S.; Sinev, I.; Bon, V.; Roldan Cuenya, B.; Kaskel, S.; Rossmeisl, J.; Strasser, P. Understanding activity and selectivity of metal-nitrogen-doped carbon catalysts for electrochemical reduction of CO_2. *Nat. Commun.* **2017**, *8*, 944.

[38] Zhang, L.; Zhao, Z. J.; Gong, J. L. Nanostructured materials for heterogeneous electrocatalytic CO_2 reduction and their related reaction mechanisms. *Angew. Chem., Int. Ed.* **2017**, *56*, 11326–11353.

[39] Ma, M.; Djanashvili, K.; Smith, W. A. Controllable hydrocarbon formation from the electrochemical reduction of CO_2 over Cu nanowire arrays. *Angew. Chem., Int. Ed.* **2016**, *55*, 6680–6684.

[40] Yang, K. D.; Ko, W. R.; Lee, J. H.; Kim, S. J.; Lee, H.; Lee, M. H.; Nam, K. T. Morphology-directed selective production of ethylene or ethane from CO_2 on a Cu mesopore electrode. *Angew. Chem., Int. Ed.* **2017**, *56*, 796–800.

[41] Liu, X. Y.; Schlexer, P.; Xiao, J. P.; Ji, Y. F.; Wang, L.; Sandberg, R. B.; Tang, M.; Brown, K. S.; Peng, H. J.; Ringe, S. et al. pH effects on the electrochemical reduction of $CO_{(2)}$ towards C_2 products on stepped copper. *Nat. Commun.* **2019**, *10*, 32.

[42] Jung, H.; Lee, S. Y.; Lee, C. W.; Cho, M. K.; Won, D. H.; Kim, C.; Oh, H. S.; Min, B. K.; Hwang, Y. J. Electrochemical fragmentation of Cu_2O nanoparticles enhancing selective C–C coupling from CO_2 reduction reaction. *J. Am. Chem. Soc.* **2019**, *141*, 4624–4633.

[43] Handoko, A. D.; Ong, C. W.; Huang, Y.; Lee, Z. G.; Lin, L. Y.; Panetti, G. B.; Yeo, B. S. Mechanistic insights into the selective electroreduction of carbon dioxide to ethylene on Cu_2O-derived copper catalysts. *J. Phys. Chem. C* **2016**, *120*, 20058–20067.

[44] Guan, B. Y., Yu, L.; Lou, X. W. General synthesis of multishell mixed-metal oxyphosphide particles with enhanced electrocatalytic activity in the oxygen evolution reaction. *Angew. Chem., Int. Ed.* **2017**, *56*, 2386–2389.

[45] Guan, B. Y.; Kushima, A.; Yu, L.; Li, S.; Li, J.; Lou, X. W. Coordination polymers derived general synthesis of multishelled mixed metal-oxide particles for hybrid supercapacitors. *Adv. Mater.* **2017**, *29*, 1605902.